An Adaptive ISAR-Imaging-Considered Task Scheduling Algorithm for Multi-Function Phased Array Radars

Yijun Chen, Qun Zhang, *Senior Member, IEEE*, Ning Yuan, *Senior Member, IEEE*, Ying Luo, *Member, IEEE*, and Hao Lou

***Abstract*—In multi-function phased array radar (MFPAR) systems, time and energy resources are allocated for different tasks so that the radar can perform various missions simultaneously. An effective scheduling algorithm is crucial to optimizing the overall performance of the MFPAR. There are various existing adaptive resource scheduling methods for the allocation of radar resources, but none of them consider the mission of imaging, a very important task. In this paper, an adaptive ISAR-imaging-considered task scheduling algorithm is proposed. Based on the sparse-aperture ISAR Compressive Sensing (CS) cognitive imaging techniques, the required resources for target imaging can be calculated from the online cognition of the target characteristics. Then the imaging mission is considered in the resource scheduling optimization model to realize adaptive allocation of radar resources and high-resolution imaging of multi targets. With the proposed algorithm, different tasks, such as tracking, searching and imaging, etc. can be implemented simultaneously, thus the radar efficiency is significantly improved. The effectiveness of the proposed method will be demonstrated by simulation experiments.**

***Index Terms*—Adaptive task scheduling algorithm, compressed sensing, inverse synthetic aperture radar imaging, phased array radar.**

Manuscript received June 07, 2014; revised October 19, 2014; accepted May 31, 2015. Date of publication June 23, 2015; date of current version August 27, 2015. The associate editor coordinating the review of this manuscript and approving it for publication was Prof. Hongwei Liu. This work was supported in part by the National Natural Science Foundation of China under Grants 61172169 and 61201369, and by the Natural Science Foundation Research Program of Shaanxi Province under Grant 2013JQ8008.

Y. Chen and H. Lou are with the Institute of Information and Navigation, Air Force Engineering University, Xi'an 710077, P. R. China, and also with the Collaborative Innovation Center of Information Sensing and Understanding, Xi'an, 710077, P. R. China (e-mail: chenyijun519@126.com; luaw2006@126.com).

Q. Zhang is with the Institute of Information and Navigation, Air Force Engineering University, Xi'an 710077, P. R. China, and also with the Collaborative Innovation Center of Information Sensing and Understanding, Xi'an, 710077, P. R. China, and the Key Laboratory for Information Science of Electromagnetic Waves (Ministry of Education), Fudan University, Shanghai 200433, P. R. China (e-mail: zhangqunnus@gmail.com).

N. Yuan is a RF Electromagnetic Engineer in Qualcomm, San Diego 92121, USA (e-mail: telebear2003@yahoo.com).

Y. Luo is with the Institute of Information and Navigation, Air Force Engineering University, Xi'an 710077, P. R. China, and also with the Collaborative Innovation Center of Information Sensing and Understanding, Xi'an, 710077, P. R. China, and the National Laboratory of Radar Signal Processing, Xidian University, Xi'an 710071, P. R. China (e-mail: luoying2002521@163.com).

Color versions of one or more of the figures in this paper are available online at http://ieeexplore.ieee.org.

Digital Object Identifier 10.1109/TSP.2015.2449251

I. Introduction

With the beam agile ability, multifunction phased array radar (MFPAR) can serve different activities such as surveillance and tracking multiple targets simultaneously [1]. Reasonable and effective resource scheduling algorithms are important for exploiting the high adaptive potential of MFPARs [2]. Among existing studies, there are mainly two ways to implement the resource management of phased array radar: template-based scheduling and adaptive scheduling [3]. Although template-based scheduling has addressed many issues in radar task scheduling, they still have some limitations in application since the templates are constructed of?ine while the resource is under-utilization [4]. Different from template-based scheduling algorithms, adaptive scheduling methods can adjust the resource scheduling strategy according to the working environment and task requirements and thus received extensive attentions. In [5], an adaptive resource management based on quality-aware was proposed to optimize the system utility. A simple but predictive heuristic algorithm proposed in [2] can reduce latency in the schedules of lateness-sensitive tasks and lessen probability of target losses.

High-resolution ISAR imaging techniques have been widely applied in military and civilian areas, such as target classification and recognition, aircraft traffic control, etc. [2], [6]. However, in almost all existing adaptive resource scheduling methods for MFPAR, the imaging mission isn't taken into account. In fact, existing MFPARs need to allocate a fixed and continuous part of time resources to implement imaging function, rather than achieve it simultaneously with tracking and searching tasks in adaptive ways. This non-adaptive allocation mode leads to the contradiction between tracking, searching tasks allocation and imaging tasks allocation. In the case of multi-target imaging, this allocation contradiction of radar resources becomes more serious. To overcome this drawback, we attempted to seek a way which can adaptively allocate radar resources for imaging without affecting the resources allocation of tracking and searching tasks as much as possible. However, achieving ISAR imaging with adaptive resource scheduling methods is not that straightforward. It will lead to discontinuousness in slow time domain of the target echoes, namely, sparse aperture, which brings trouble to traditional ISAR imaging. Linear-prediction extrapolation or modern spectral estimation can be used to approximate the complete echo information of a target, but these methods will

introduce large errors when the aperture loss is large [7], so it is required to seek a novel solution for ISAR imaging with adaptive resource scheduling methods.

An emerging theory called Compressive Sensing (CS) provides a new method for sparse-aperture ISAR imaging. Compressed Sensing was proposed by D. Donoho, E. Candès, T. Tao, *et al.* [8], [9]. It can recover a sparse or compressible signal from far fewer measurements than what the Nyquist sampling theory claimed with high probability, by exploiting the signal sparsity [8]–[11]. The work in [10] introduced CS into high resolution range profile (HRRP) synthesis through sparse stepped-frequency waveforms and reconstructed full-resolution image. An ISAR imaging algorithm based on CS is proposed in [12] to estimate the locations of the scattering centers from a very limited number of measurements. These methods leave open the possibility that ISAR images can be accomplished with adaptive resource scheduling algorithm. By inserting imaging pulses into the interval between tracking and searching tasks, ISAR imaging can be realized without affecting target tracking and searching. Apparently, the efficiency of the radar can be improved significantly.

In this paper, we propose an adaptive ISAR-imaging-considered task scheduling algorithm based on the sparse-aperture ISAR CS imaging techniques. In the proposed algorithm, the cognitive imaging technology proposed in [13], [14] is utilized to realize high-resolution imaging of multi targets and adaptive allocation of radar resources. Based on the online cognition of the target characteristics, the radar resource is allocated according to different priorities, required azimuth observation dimension and observation time calculated by the feedback information from the cognition. As a result, the high-quality ISAR imagery is obtained without affecting tracking and searching tasks, thus the overall efficiency of the radar is improved significantly.

This paper is organized as follows. The CS theory and sparse-aperture ISAR imaging based on CS are introduced in Section II. The adaptive scheduling algorithm based on sparse-aperture cognitive ISAR imaging is proposed in Section III. Simulations are presented in Section IV to validate the effectiveness of the proposed algorithm, followed by some discussions and conclusions in Section V.

II. Sparse-Aperture ISAR Imaging Based on Compressed Sensing

The sparse-aperture ISAR imaging method based on compressed sensing have been discussed comprehensively in existing literatures [12], [15]. For completeness of the content, we briefly introduce the CS-based sparse-aperture ISAR imaging algorithm in this section.

The basic idea of the compressed sensing theory is that a sparse signal can be exactly recovered from a very limited number of measurements with high probability by exploiting the sparsity of the signal via solving a sparsity-constrained optimization problem [9], [16]. The CS theory mainly includes three contents, sparse representation of the signal [17], measurement matrix design [18], and signal reconstruction algorithm [19]–[22].

The CS has been successfully used for ISAR imaging with the advantage of data quantity decrement. The sparse aperture ISAR imaging algorithm based on CS can be described as follows. Scatterer model is usually employed to describe a radar target in radar imaging [14]. Without loss of generality, we assume the ISAR target contains P scatterers. The radar transmits linear frequency modulated (LFM) signals, and it requires azimuthal coherent accumulation time T_c to obtain the desired azimuthal resolution, then $N_{all} = PRF \cdot T_c$ pulses are transmitted during the imaging time, where PRF denotes the pulse repetition frequency. The full aperture echo signal can be written as

$$s(t,\tau_m) = \sum_{p=1}^{P} \sigma_p \exp\left\{ j2\pi \left[f_c \left(t - \frac{2R_p(\tau_m)}{c} \right) + \frac{1}{2}\mu \left(t - \frac{2R_p(\tau_m)}{c} \right)^2 \right] \right\}, t \in \left[-\frac{T_p}{2}, \frac{T_p}{2} \right], m = 1, 2, \ldots, N_{all} \tag{1}$$

where t is fast time, τ_m is the sampling sequence of slow time and there are N_{all} sampling points. T_p, f_c, μ and σ_p are the pulse duration, the carrier frequency, the chirp rate and the scattering coefficient of the p-th scattering points, respectively. $R_p(\tau_m)$ is the distance between the p-th scattering point and radar at τ_m.

Due to the change in work status or practical application, the radar only launches $M_s (M_s < N_{all})$ sub-pulses to the target, thus the sparse aperture signal can be written as:

$$s(t,\tau_m) = \sum_{p=1}^{P} \sigma_p \exp\left\{ j2\pi \left[f_c \left(t - \frac{2R_p(\tau_m)}{c} \right) + \frac{1}{2}\mu \left(t - \frac{2R_p(\tau_m)}{c} \right)^2 \right] \right\}, m' = 1, 2, \ldots, M_s \tag{2}$$

After performing range compression and neglecting the migration through the range cell, we have the sparse aperture signal as follows:

$$s_r(f,\tau_{m'}) = T_p \sum_{p=1}^{P} \sigma_p \mathrm{sinc}\left(T_p \left(f + \frac{2\mu}{c} \cdot \Delta R_{p0} \right) \right) \cdot \exp\left(-j\frac{4\pi}{c} f_c \cdot \Delta R_p(\tau_{m'}) \right), m' = 1, 2, \ldots, M_s \tag{3}$$

where $\Delta R_p(\tau_{m'}) = R_p(\tau_{m'}) - R_0(\tau_{m'})$, $R_0(\tau_{m'})$ is the distance between the reference point and the radar at $\tau_{m'}$, ΔR_{p0} is the distance between the reference point and the p-th scattering point at the beginning of imaging.

Traditional imaging algorithms for full aperture of ISAR usually apply the Fourier transform with respect to τ_m to obtain the 2D target image. Usually, the ISAR image is mainly determined by some dominant scatterers, so the echo of the target can be regarded as sparse in the azimuthal (Doppler) domain. Thus, the CS theory can be used to implement sparse-aperture ISAR imaging. Choose N_{all}-dimensional inverse DFT matrix as $\mathbf{\Psi}$, and design a $M_s \times N_{all}$ matrix $\mathbf{\Phi}$ according to the sub-aperture allocation:

$$\phi_{m',m} = \begin{cases} 1, & \{(m',m) | \tau_{m'} = \tau_m\} \\ 0, & else \end{cases} \tag{4}$$

It can be readily proved that $\mathbf{\Psi}$ and $\mathbf{\Phi}$ are incoherent [13], therefore the azimuthal information can be reconstructed by the optimization algorithm

$$\Theta = \min \left\| \mathbf{\Psi}\mathbf{\Phi}^H S_r(f,\tau_m) \right\|_1, \quad s.t.\ S_r(f,\tau_m) = \mathbf{\Phi} X = \mathbf{\Phi}\mathbf{\Psi}^H \Theta \tag{5}$$

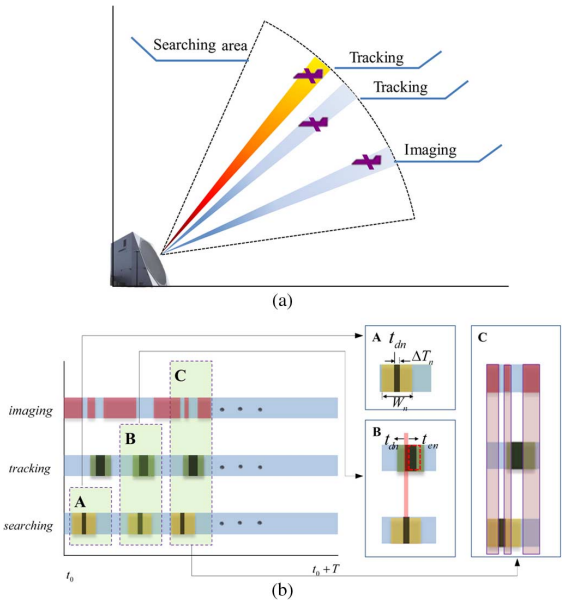

Fig. 1. Radar resource scheduling diagram. (a) Scenario. (b) Time sequence.

The object function Θ is the expected azimuthal image of the target, and we can obtain the 2D ISAR image by using the method above for each range cell to get the azimuthal image and then arranging them into a matrix.

III. ISAR-Imaging-Considered Adaptive Radar Resource Scheduling Strategy

As mentioned before, in a MFPAR system, radar serves different activities in its surveillance space [4]. Therefore, an effective scheduling strategy is required to allocate the radar resources in a way that the global utility of MFPAR is maximized. And the radar resource scheduling diagram is shown in Fig. 1.

Fig. 1(a) shows the process that the radar implements searching task in the searching area at searching update rate. With the beam agile ability, the tracking and imaging of the detected targets can be implemented at any required time. The red wave beam in Fig. 1(a) denotes the current position of the radar wave which is tracking the target. The blue wave beams represent that the radar will implement the tracking and imaging for other targets soon.

Obviously, there is conflict of radar resource allocation between different tasks. The goal of the adaptive task scheduling algorithm is to avoid the conflict and achieve the maximized global utility of MFPAR. For the sake of simplicity, we only consider searching, tracking and imaging tasks in this subsection, and the time sequence of task scheduling is shown as in Fig. 1(b), where the scheduling interval is set as $[t_0, t_0 + T]$. In Part A of Fig. 1(b), t_{dn} is the expected execution time of the n-th task, the black vertical bar represents the dwell time ΔT_n, and the yellow region denotes the time window W_n (the range of back-and-forth motion between the expected execution time and the actual execution time), respectively. Part B of Fig. 1(b) shows the conflict between the tracking and searching tasks. To implement both tasks at their expected execution time, the time slot shown as red vertical bar is needed by both two tasks, so the task with lower priority can't be implemented at its expected execution time t_{dn}, and its actual execution time t_{en} should be moved in the time window. In practice, when the searching and tracking task request is not too large, there will be a small amount of unoccupied time slots in a scheduling interval. These vacant time slot can be allocated for target imaging with sparse observations, and then the 2D high-resolution ISAR image can be obtained using the sparse-aperture imaging method based on the CS. And the imaging resources allocation is shown in Part C of Fig. 1(c), in which the red vertical bar represents the vacant time slot and be used for target imaging.

However, almost all existing adaptive resource scheduling methods did not consider the imaging function. Based on the CS-ISAR, an adaptive radar resource scheduling strategy is proposed in this section. We will first briefly introduce the traditional adaptive scheduling strategy for MFPAR, and then expatiate the proposed ISAR-imaging-considered adaptive radar resource scheduling strategy in detail.

A. Traditional Adaptive Scheduling Strategy For MFPAR

First, consider the traditional time-window-based task scheduling approach for MFPARs. Assume T is the length of the scheduling interval, set $A = \{A_1, A_2, \ldots, A_{Nt}\}$ depicts Nt tasks including high-priority search (HS), precision track (PT), normal track (NT) and low-priority search (LS) during the scheduling interval $[t_0, t_0 + T]$. P_n is the priority of the n-th task, and other symbols (such as t_{dn}, t_{en}, ΔT_n and W_n) are the same as in Fig. 1. The scheduling optimization model can be written as follows [23]:

$$\begin{aligned} &\max\{\sum_{n=1}^{NT} P_n \cdot U(t_0 + T - t_{en} - \Delta T_n)\} \\ st.\ &\max(t_0, t_{dn} - W_n) \le t_{en} \le \min(t_{dn} + W_n, t_0 + T - \Delta T_n) \\ &\min(t_{en'} - t_{en}) \ge \Delta T_n, n' \in \{n' | t_{en'} > t_{en}\} \end{aligned} \tag{6}$$

where $U(x) = \begin{cases} 1 & x \ge 0 \\ 0 & x < 0 \end{cases}$.

We can get the tasks implement sequence by solving the optimization problem.

Generally, in ascending order of priority, the sequence of these tasks is: low-priority search, normal track, precision track and high-priority search [24].

B. ISAR-Imaging-Considered Adaptive Radar Resource Scheduling

The time-window-based task scheduling approach described in the previous section does not consider the impact of the imaging function on the resources scheduling strategy and needs a fixed and continuous part of resource for imaging while accomplishing the searching and tracking activities. As a result, the working efficiency of radar is not high.

In practice, when the searching and tracking task request is not too large, there will be a small amount of unoccupied time slots in a scheduling interval after the adaptive resource scheduling. These vacant time slot can be allocated for target imaging with sparse observations, and then the 2D high-resolution ISAR image can be obtained using the sparse-aperture imaging method based on the CS.

As we know, azimuthal coherent accumulation time is absolutely necessary for ISAR imaging, and the coherent accumulation time depends on the relative rotation angle of the radar and the target as well as the desired azimuthal resolution. In

other words, target characteristics will constraint to the allocation of resources. Therefore, the ideal way to allocate the resources effectively for realizing sparse-aperture imaging of targets is to do it adaptively according to the target characteristics. Therefore, the cognitive imaging technology proposed in [11], [12] is introduced into the adaptive resource scheduling strategy. First, radar cognizes the target characteristics (distance, speed, heading, size, sparsity of echo in Doppler domain, etc.) by transmitting a small amount of pulses, and then calculates the imaging priority and the measurement dimensions (i.e., the number of sampling points in slow-time domain) according to the feedback information. For example, a target which is closer and moving toward the radar at high speed is considered more threatening, thus has higher priority. Furthermore, the measurement dimension can be determined according to the estimation of the sparsity of the echo in Doppler domain. On this basis, a rational time resource allocation strategy can implement searching, tracking and imaging at the same time.

The distance $\hat{R}_k$, speed $\hat{V}_k$ and heading $\hat{\theta}_k$ can be measured using conventional tracking algorithms. Evaluation of the size $\hat{S}_k$, sparsity $\hat{K}_{k,l}$ of echo in Doppler domain, priority $P_{k,l}$, the desired measurement dimension $M_{k,l}$ and the ending time of each imaging task will be explained one by one in the following paragraphs.

(1) To estimate the target size $\hat{S}_k$ of the k-th imaging task. For the sake of simplicity, we assume there is only a single non-maneuvering target for ISAR imaging in each imaging task. The coarse-resolution ISAR image of the k-th imaging task $s_{pk}(f, f_{\tau_m})$ can be obtained by transmitting a small amount of pulses with uniform intervals. The normalization of the ISAR image can be written as

$$s'_{pk}(f, f_{\tau_m}) = \frac{|s_{pk}(f, f_{\tau_m})| - \max\limits_{f, f_{\tau_m}} |s_{pk}(f, f_{\tau_m})|}{\max\limits_{f, f_{\tau_m}} |s_{pk}(f, f_{\tau_m})| - \min\limits_{f, f_{\tau_m}} |s_{pk}(f, f_{\tau_m})|} \quad (7)$$

Setting a proper threshold T_s and letting $f_{small} = \min\limits_f\{f | s'_{pk}(f, f_{\tau m}) > T_s\}$, $f_{big} = \max\limits_f\{f | s'_{pk}(f, f_{\tau m}) > T_s\}$, we can get the range size of the k-th target based on the linear relation between the frequency and distance: $\hat{S}_{ky} = \frac{c}{2\mu}(f_{big} - f_{small}) = (f_{big} - f_{small}) \cdot T_p \cdot \rho_r$, where ρ_r is the range resolution. Similarly we can get the azimuthal size $\hat{S}_{kx} = (f_{\tau_m big} - f_{\tau_m small}) \cdot T_c \cdot \rho_c$, where ρ_c is the azimuthal resolution, and it can be determined from the estimation of distance $\hat{R}_k$, speed $\hat{V}_k$ and heading $\hat{\theta}_k$ according to the equation $\rho_c = \lambda \hat{R}_k / 2\hat{V}_k \cos\hat{\theta}_k$. Therefore, the size of the k-th target is $\hat{S}_k = \hat{S}_{kx} \cdot \hat{S}_{ky}$.

(2) To estimate the sparsity $\hat{K}_{k,l}$ of Doppler-domain echo in l-th scheduling interval of the k-th imaging task. The initial estimation of $\hat{K}_{k,0}$ can be obtained by normalizing $s_{pk}(f, f_{\tau_m})$ as follows:

$$s''_{pk}(f_{\tau_m}) = \frac{\max\limits_f |s_{pk}(f, f_{\tau_m})| - \max\limits_{f_{\tau_m}} \left\{ \max\limits_f |s_{pk}(f, f_{\tau_m})| \right\}}{\max\limits_{f_{\tau_m}} \left\{ \max\limits_f |s_{pk}(f, f_{\tau_m})| \right\} - \min\limits_{f_{\tau_m}} \left\{ \max\limits_f |s_{pk}(f, f_{\tau_m})| \right\}} \quad (8)$$

Setting a proper threshold T_k and letting vector s''_{pk} be the discrete representation of $s''_{pk}(f_{\tau m})$, $\hat{K}_{k,0}$ is defined as the number of elements which are greater than T_k in s''_{pk}.

However, the estimation of $\hat{K}_{k,0}$ is not precise enough and needs to be updated in the imaging process. Assume $s_{k,l}(f, f_{\tau m})$ denote the complex ISAR image of the k-th imaging task obtained by all the transmitted pulses until the end of the l-th scheduling interval. Normalize $s_{k,l}(f, f_{\tau m})$ as follows:

$$s'_{k,l}(f_{\tau_m}) = \frac{\max\limits_f |s_{k,l}(f, f_{\tau_m})| - \max\limits_{f_{\tau_m}} \left\{ \max\limits_f |s_{k,l}(f, f_{\tau_m})| \right\}}{\max\limits_{f_{\tau_m}} \left\{ \max\limits_f |s_{k,l}(f, f_{\tau_m})| \right\} - \min\limits_{f_{\tau_m}} \left\{ \max\limits_f |s_{k,l}(f, f_{\tau_m})| \right\}} \quad (9)$$

Letting vector $s'_{k,l}$ be the discrete representation of $s'_{k,l}(f_{\tau_m})$, the $\hat{K}_{k,l}$ is defined as the number of elements which are greater than T_k in $s'_{k,l}$.

Based on the estimation of $\hat{R}_k$, $\hat{V}_k$, $\hat{\theta}_k$ and $\hat{K}_{k,l}$, the priority and required measurement dimension can be determined by the following steps.

(3) To determine the priority $P_{k,l}$ in the l-th scheduling interval of the k-th imaging task. Without loss of generality, the target with closer distance, higher speed and moving toward the radar is more threatening and requires a higher priority, thus the initial priority of each target can be given by

$$P_{k,0} = p_a \left(1/\hat{R}_k\right)' + p_b \hat{V}'_k + p_c \left(\sin\hat{\theta}_k\right)', \quad p_a, p_b, p_c \geq 0, p_a + p_b + p_c = 1 \quad (10)$$

where

$$\left(1/\hat{R}_k\right)' = \frac{1/\hat{R}_k}{\max\left(1/\hat{R}_k\right)}, \hat{V}'_k = \frac{\hat{V}_k}{\max\left(\hat{V}_k\right)},$$
$$\left(\sin\hat{\theta}_k\right)' = \frac{\sin\hat{\theta}_k}{\max\left(\sin\hat{\theta}_k\right)}$$

and p_a, p_b, and p_c are the adjustment factors representing the impact degree of different characteristics on the priority. Obviously, the initial priority of imaging task is $P_{k,0} \in [0, 1]$, which is ensured to be lower than the priority of high-priority search tasks (with priority of 4), precision track tasks (with priority of 3), normal track tasks (with priority of 2) and low-priority search tasks (with priority of 1). However, due to the azimuthal coherent accumulation time is much bigger than the scheduling interval T, several scheduling intervals are usually required to accomplish an imaging task. To avoid waste of the pulses transmitted for imaging, we adopt a dynamic priority adjustment strategy for imaging tasks. In this strategy, if the k-th imaging task is implemented in the l-th scheduling interval, the priority of this task will be improved appropriately in the next scheduling interval:

$$P_{k,l+1} = P_{k,l} + \Delta P \quad (11)$$

where ΔP is the step of the priority. It should be noted that the number of searching and tracking tasks in the working area of MFPAR almost keep stable during a short time period. However, for imaging task, as the azimuthal coherent accumulation time increases, the resolution of ISAR image and the estimation accuracy of sparsity increase accordingly, and the required measurement dimensions decrease. In a word, if an imaging task

is implemented in the i-th scheduling interval, it can be implemented in the next scheduling interval with high probability. Therefore, the radar resource will not be wasted.

(4) To determine the measurement dimension $M_{k,l}$ in the l-th scheduling interval of the k-th imaging task. According to the CS theory, OMP algorithm can reconstruct the original signal with high probability when the measurement dimension meets the constraint $M \geq c_1 K \ln(N)$, where c_1 is a coefficient between 0.5 and 2 [12], thus the required measurement dimension in a single scheduling interval of each target is determined by

$$M_{k,l} \geq \frac{c_1 \hat{K}_{k,l-1} \ln(N_{T_{ck}})}{T_{ck}/T} \tag{12}$$

where $N_{T_{ck}} = T_{ck} \cdot PRF$, T_{ck} is the azimuthal coherent accumulation time of the k-th imaging task to obtain the desired azimuthal resolution. Generally speaking, larger targets require lower resolution while smaller targets need higher resolution for precise imaging, so the azimuthal coherent accumulation time T_{ck} of the k-th imaging task is determined by

$$T_{c,k} = \left(S_{refx} \cdot \hat{R}_k \cdot \lambda\right) / \left(\hat{S}_{kx} \cdot \hat{V}_K \left|\cos(\hat{\theta}_K)\right| \cdot 2\rho_{ref}\right) \tag{13}$$

where ρ_{ref} is the desired azimuthal resolution of the target with datum azimuthal size of S_{refx}. What should be pointed out is that according to the sparse-aperture ISAR imaging algorithm based on CS, the launching time $t_{eM_{k,l}}$ of these $M_{k,l}$ pulses for imaging should be a multiple of $1/PRF$.

(5) To determine the ending time of each imaging task.

For multiple imaging tasks, the required coherent accumulation time for each target is different. Therefore the utilization rate of the radar time resource can be improved by making use of the closed feedback loop between the receiver and transmitter to adjust the imaging accumulation time for each target.

Generally, as the azimuthal coherent accumulation time increases, the quality of ISAR image will increase accordingly and gradually comes to a standstill. After reaching the standstill, the quality of ISAR image will be worse if the azimuthal coherent accumulation time continues to increase. Therefore, we can determine the ending time of each imaging task by measuring the correlation coefficients of two adjacent reconstructed ISAR images, $s_{k,l}(f, f_{\tau m})$ and $s_{k,l+1}(f, f_{\tau m})$, which can be given by

$$\alpha = \frac{\int |S_{k,l+1}(:, f_{\tau m})| \, |S_{k,l}(:, f_{\tau m})| \, \mathrm{d}f_{\tau m}}{\sqrt{\int |S_{k,l+1}(:, f_{\tau m})|^2 \, \mathrm{d}f_{\tau m} \cdot \int |S_{k,l}(:, f_{\tau m})|^2 \, \mathrm{d}f_{\tau m}}} \tag{14}$$

If the correlation coefficient is relatively small, the similarity of ISAR images from the adjacent scheduling intervals is relatively low. In this case, the image quality need to be improved by going on transmitting pulses in the next scheduling interval. On the contrary, if the correlation coefficient is relatively large, the image quality can be hardly improved by going on transmitting pulses. Therefore, we need to select an appropriate threshold to control this procedure. When the correlation coefficient of the ISAR images between the adjacent two scheduling intervals is less than the threshold, the imaging task will continue to be executed in the next scheduling interval. Otherwise, we think the image quality has reached the expected standard and the task finishes.

On this basis, three performance metrics are used to evaluate the effectiveness of the resource scheduling algorithm:

(1) The sum of the priority of the implemented tasks (SPI) in each scheduling interval, defined by

$$SPI = \sum_{n=1}^{N_{\mathrm{sts}}} P_n + \sum_{k=1}^{N_{\mathrm{ims}}} P_{k,l} \tag{15}$$

where N_{sts} is the number of implemented searching and tracking tasks in the scheduling interval, N_{ims} is the number of implemented imaging task in the scheduling interval.

(2) The ratio of the implemented tasks to the total tasks (ROI) in each scheduling interval, defined by

$$ROI = \left(N_{\mathrm{sts}} + N_{\mathrm{ims}}\right) / N_a \tag{16}$$

where N_a is the number of the total tasks in the scheduling interval.

(3) Time utilization rate (TUR) of each scheduling interval, defined by

$$TUR = \left(\sum_{n=1}^{N_{\mathrm{sts}}} \Delta T_n + \sum_{k=1}^{N_{\mathrm{ims}}} M_{k,l}/PRF\right) / T \tag{17}$$

In view of the above performance metrics, the resource scheduling optimization model based on sparse-aperture ISAR imaging is proposed as:

$$\begin{aligned} &\max\left\{\omega_1 SPI + \omega_2 ROI + \omega_3 TUR\right\} \\ &s.t.\ for\ searching\ and\ tracking, \\ &\quad \begin{cases} \max(t_0, t_{dn} - W_n) \leq t_{en} \\ t_{en} \leq \min(t_{dn} + W_n, t_0 + T - \Delta T_n) \\ \min(t_{en'} - t_{en}) \geq \Delta T_n, \\ n' \in \{n' | t_{en'} > t_{en} \end{cases} \\ &\quad for\ imaging, t_{eM_{k,l}} = z/PRF, z \in N^+ \\ &\quad \sum_{n=1}^{N_{\mathrm{sts}}} \Delta T_n + \sum_{k=1}^{N_{\mathrm{ims}}} M_{k,l}/PRF \leq T \end{aligned} \tag{18}$$

Where ω_1, ω_2, and ω_3 are the adjustment factors representing the impact degree of different performance metrics on the scheduling algorithm. Other parameters are the same as in (6) and (12).

The concrete steps of the adaptive scheduling algorithm for radar resource based on sparse-aperture ISAR imaging can be summarized as follows:

Step 1) Transmit a small amount of pulses to the imaging targets that have been scanned by radar, and initially cognize the characteristics of the targets (distance $\hat{R}_k$, speed $\hat{V}_k$, size $\hat{S}_k$ and initial sparsity $\hat{K}_{k,0}$) according to the echo signal, then initialize the measurement matrix $\mathbf{\Phi}_0 = \emptyset$;

Step 2) Calculate the sparsity, priority and the required measurement dimension of the targets in a certain scheduling interval according to (9)–(13);

Step 3) Step 3: Allocate the time resource of radar for the l-th scheduling interval according to the scheduling optimization model in (18), the concrete method is described as follows:

The implemented benefit of each task (i.e., the obtained benefit of implementing each task) is defined as:

$$\begin{aligned} &for\ searching\ and\ tracking,\\ &Q_n = \omega_1 P_n' + \omega_2 (T/\Delta T_n)' + \omega_3 (\Delta T_n/T)'\\ &\quad for\ imaging,\\ &Q_k = \omega_1 P_{k,l}' + \omega_2 \left(\frac{T}{M_{k,l}/PRF}\right)' + \omega_3 \left(\frac{M_{k,l}/PRF}{T}\right)' \end{aligned} \tag{19}$$

where

$$\begin{aligned} &P_n' = P_n/\max(P_n, P_{k,l}), P_{k,l}' = P_{k,l}/\max(P_n, P_{k,l})\\ &(T/\Delta T_n)' = \frac{T/\Delta T_n}{\max(T/\Delta T_n, T/(M_{k,l}/PRF))},\\ &(T/(M_{k,l}/PRF))' = \frac{T/(M_{k,l}/PRF)}{\max(T/\Delta T_n, T/(M_{k,l}/PRF))}\\ &(\Delta T_n/T)' = \frac{\Delta T_n/T}{\max(\Delta T_n/T, (M_{k,l}/PRF)/T)},\\ &((M_{k,l}/PRF)/T)' = \frac{(M_{k,l}/PRF)/T}{\max(\Delta T_n/T, (M_{k,l}/PRF)/T)} \end{aligned}$$

Because the dwell time of searching and tracking tasks is a multiple of $1/PRF$ and the imaging tasks are not restricted to the time window, we can only reserve apertures for the imaging tasks instead of arranging the actual execution time for them. Then the reserved vacant apertures are used for implementing imaging tasks after the actual execution time of searching and tracking tasks are determined. The concrete approach of allocating the time resources according to the scheduling optimization model (18) is depicted as follows.

Calculating the implemented benefit of each task in the l-th scheduling interval, the waiting task set $A' = \{A_1', A_2', \ldots, A_{N_a}'\}$ can be obtained by sorting the benefit from high to low. Each task $A_s'(s = 1, 2, \ldots N_a)$ can be analyzed to judge whether it is to be implemented and what the actual execution time $t_{eA_s'}$ is if it is to be implemented.

Assume that there are N_s searching and tracking tasks confirmed to be implemented before the analysis of A_s'. $B' = \{B_1', B_2, \ldots, B_{N_S}'\}$ is the implemented tasks set by sorting these searching and tracking tasks according to the execution time.

Case 1) If A_s' is a searching task or tracking task, first we need to find B_h' and B_{h+1}' (in the set of B') whose execution time $t_{eB_h'}$ and $t_{eB_{h+1}'}$ are closest (before or after) to the expected execution time $t_{dA_s'}$ of A_s'. The necessary and sufficient condition that A_s' can be implemented is:

$$\begin{aligned} &t_{eB_{h+1}'\_l} - t_{eB_h'\_f} \geq \Delta T_{A_s'} + \Delta T_{B_h'},\\ &\Delta T_{A_s'} + \sum_{h=1}^{N_S} \Delta T_{B_h'} + \Delta T_{imaging} \leq T \end{aligned} \tag{20}$$

where $\Delta T_{imaging}$ is the sum of the required dwell time of all imaging tasks which have been confirmed to be implemented. $t_{eB_h'\_f} = \max\{t_{dB_h'} - W_{B_h'}, t_{eB_{h-1}'} + \Delta T_{B_{h-1}'}\}$ represents the earliest execution time of B_h', on the contrary, $t_{eB_{h+1}'\_l} = \min\{t_{dB_{h+1}'} + W_{B_{h+1}'}, t_{eB_{h+2}'} - \Delta T_{B_{h+1}'}\}$ stands for the latest execution time of B_{h+1}'.

When A_s' satisfies (20), we think it can be implemented. The actual execution time $t_{eA_s'}$ of A_s' can be determined as follows.

a. Assume the actual execution time $t_{eB_h'}$ and $t_{eB_{h+1}'}$ of B_h' and B_{h+1}' are fixed at first, the actual execution time $t_{eA_s'}$ of A_s' can be calculated by:

$$\min |t_{eA_s'} - t_{dA_s'}| \quad st. \begin{cases} t_{eA_s'} - t_{eB_h'} \geq \Delta T_{B_h'}\\ t_{eB_{h+1}'} - t_{eA_s'} \geq \Delta T_{A_s'}\\ |t_{eA_s'} - t_{dA_s'}| \leq W_{A_s'} \end{cases} \tag{21}$$

b. If a $t_{eA_s'}$ satisfying (21) does not exist when $t_{eB_h'}$ and $t_{eB_{h+1}'}$ are fixed, we can bring forward the actual execution time $t_{eB_h'}$ and postpone the actual execution time $t_{eB_{h+1}'}$ gradually until a $t_{eA_s'}$ satisfying (21) exists. The value of $t_{eA_s'}$ is then determined according to (21).

Case 2) If A_s' is an imaging task, we only judge whether or not it is to be implemented and do not arrange the actual execution time for it. The task A_s' will be implemented when the condition $M_{A_s',l}/PRF + \sum_{h=1}^{N_S} \Delta T_{B_h'} + \Delta T_{imaging} \leq T$ is satisfied. Otherwise, A_s' will not be implemented. If A_s' is confirmed to be implemented, $\Delta T_{imaging}$ should be updated as $\Delta T_{imaging} = \Delta T_{imaging} + M_{A_s',l}/PRF$.

After analyzing all waiting tasks, the sub-pulses of all the imaging tasks confirmed to be implemented are randomly arranged in the reserved vacant apertures. Thus, the time resource allocation of the l-th scheduling interval is completed. It should be noted that the process above just use one-step backtracking. Two or more step backtracking can be used when required but will lead to more computation load.

Step 4: Structure the measurement matrix $\mathbf{\Phi}_l'$ according to the distribution of the allocated sub-aperture, and then the measurement matrix under the framework of compressed sensing after the l-th scheduling interval can be written as $\mathbf{\Phi}_l = [\mathbf{\Phi}_{l-1}, \mathbf{\Phi}_l']$;

Step 5: Use the sparse-aperture ISAR imaging method based on CS for target imaging and calculate the correlation coefficient of the ISAR images from the two adjacent scheduling intervals. When the correlation coefficient is more than the predefined threshold, set the implemented benefit of the imaging task to zero and this task is no longer scheduled in the next scheduling interval. Otherwise, put the imaging task into the next scheduling interval for analysis.

Step 6: Repeat from Step 2 and allocate the radar resource for the next scheduling interval.

C. Probability Analysis of ROI=1 in a Certain Scheduling Interval

Assume that there are N_{HS} high-priority searching tasks $(A_1, A_2, \ldots, A_{N_{HS}})$, M_{PT} precision tracking tasks $(B_1, B_2, \ldots, B_{M_{PT}})$, U_{NT} normal tracking tasks $(C_1, C_2, \ldots, C_{U_{NT}})$, G_{LS} low-priority searching tasks $(D_1, D_2, \ldots, D_{G_{LS}})$ and V_{IT} imaging tasks $(E_1, E_2, \ldots, E_{V_{IT}})$ to be scheduled during the l-th scheduling interval $[t_0, t_0 + T]$. The dwell time of high-priority searching, precision tracking, normal tracking and low-priority

TABLE I
PROBABILITY-LAW DISTRIBUTION OF TASK DURATION ΔT

Task duration ΔT	ΔT_a	ΔT_b	ΔT_c	ΔT_d
Probability P	$N_{HS}/N_{HS}+M_{PT}+U_{NT}+G_{LS}$	$M_{PT}/N_{HS}+M_{PT}+U_{NT}+G_{LS}$	$U_{NT}/N_{HS}+M_{PT}+U_{NT}+G_{LS}$	$G_{LS}/N_{HS}+M_{PT}+U_{NT}+G_{LS}$

searching are ΔT_a, ΔT_b, ΔT_c and ΔT_d, respectively. And the corresponding time window are W_a, W_b, W_c and W_d, respectively. T_{aq}, T_{bq}, T_{cq} and T_{dq} are random variables that denote the expected execution time of the q-th high-priority searching task, precision tracking task, normal tracking task and low-priority searching task, respectively.

Obviously, the probability of $ROI = 1$ in l-th scheduling interval is zero when $N_{HS}\cdot\Delta T_a + M_{PT}\cdot\Delta T_b + U_{NT}\cdot\Delta T_c + G_{LS}\cdot\Delta T_d + \sum_{k=1}^{V_{IT}} M_{k,l}/PRF > T$. On the contrary, when the tasks satisfy $N_{HS}\cdot\Delta T_a + M_{PT}\cdot\Delta T_b + U_{NT}\cdot\Delta T_c + G_{LS}\cdot\Delta T_d + \sum_{k=1}^{V_{IT}} M_{k,l}/PRF \le T$, the probability of $ROI = 1$ in l-th scheduling interval can be calculated as:

$$\begin{aligned} P_{ROI=1} &= P(A_1\cdots A_{N_{HS}}B_1\cdots B_{M_{PT}}C_1\cdots \\ &\qquad C_{U_{NT}}D_1\cdots D_{G_{LS}}E_1\cdots E_{V_{IT}}) \\ &= P(\text{condition1}, \text{condition2}, \cdots, \text{condition11}) \end{aligned} \tag{22}$$

where the 11 conditions (as shown in the Appendix) guarantee there is no conflict between any tasks.

Solving (22) involves a multiple integral and is very complicated. Here we introduce the queuing theory to obtain $P_{ROI=1}$.

Without loss of generality, suppose that task arrival is a Poisson process having rate $\lambda = N_{HS}+M_{PT}+U_{NT}+G_{LS}/T$, and the probability-law distribution of the task duration ΔT is shown as Table I.

Because imaging tasks just make use of the vacant aperture and is not restricted to time window, when it satisfies $N_{HS}\cdot\Delta T_a + M_{PT}\cdot\Delta T_b + U_{NT}\cdot\Delta T_c + G_{LS}\cdot\Delta T_d + \sum_{k=1}^{V_{IT}} M_{k,l}/PRF \le T$, we can only queue the searching and tracking tasks.

Assume X_r is the number of tasks in the queue after the r-th task accomplished, and Y_r is the number of arrival tasks during the r-th task.

Define

$$J = 2\overline{W}/\overline{\Delta T} \tag{23}$$

where

$$\begin{aligned} \bar{W} &= \frac{(N_{HS}W_a + M_{PT}W_b + U_{NT}W_c + G_{LS}W_d)}{(N_{HS}+M_{PT}+U_{NT}+G_{LS})} \\ \overline{\Delta T} &= \frac{(N_{HS}\Delta T_a + M_{PT}\Delta T_b + U_{NT}\Delta T_c + G_{LS}\Delta T_d)}{(N_{HS}+M_{PT}+U_{NT}+G_{LS})} \end{aligned}$$

When the number of waiting tasks is larger than J, there must be a task can't be implemented and departed, so the state room of X_r is $E = \{0, 1, 2, \ldots, J\}$.

It can be proved that $\{X_r, r \ge 1\}$ is a Markov chain, $Y_1, Y_2, \cdots$ are independent and identically distributed. Assuming

$$p_\beta = P\{Y_1 = \beta\}, \beta = 0, 1, 2, \cdots \tag{24}$$

Since task arrival is a Poisson process having rate λ, p_β can be calculated as:

$$\begin{aligned} p_\beta = &\frac{N_{HS}}{N_{HS}+M_{PT}+U_{NT}+G_{LS}}\cdot\frac{(\lambda\Delta T_a)^\beta}{\beta!}\cdot\exp(-\lambda\Delta T_a) \\ &+\frac{M_{PT}}{N_{HS}+M_{PT}+U_{NT}+G_{LS}}\cdot\frac{(\lambda\Delta T_b)^\beta}{\beta!}\cdot\exp(-\lambda\Delta T_b) \\ &+\frac{U_{NT}}{N_{HS}+M_{PT}+U_{NT}+G_{LS}}\cdot\frac{(\lambda\Delta T_c)^\beta}{\beta!}\cdot\exp(-\lambda\Delta T_c) \\ &+\frac{G_{LS}}{N_{HS}+M_{PT}+U_{NT}+G_{LS}}\cdot\frac{(\lambda\Delta T_d)^\beta}{\beta!}\cdot\exp(-\lambda\Delta T_d) \end{aligned} \tag{25}$$

Define

$$p_{ij}(r,1) = P\{X_{r+1} = j | X_r = i\} \tag{26}$$

Then we have

$$p_{ij}(r,1) = 0, i > j+1, i < J \tag{27}$$

$$p_{ij}(r,1) = p_j, i = 0, j < J \tag{28}$$

$$p_{ij}(r,1) = \sum_{j=J}^{\infty} p_j, i = 0, j = J \tag{29}$$

$$p_{ij}(r,1) = p_{j-i+1}, 0 < i \le j+1, j < J \tag{30}$$

$$p_{ij}(r,1) = \sum_{j=J}^{\infty} p_{j-i+1}, 0 < i \le j+1, j = J \tag{31}$$

Because $p_{ij}(r,1)$ is independent of r, $\{X_r, r \ge 1\}$ is a homogeneous Markov chain, the matrix of one-step transition probabilities p_{ij} is

$$p = \begin{bmatrix} p_0 & p_1 & \cdots & p_{J-1} & \sum_{j=J}^{\infty} p_j \\ p_0 & p_1 & \cdots & p_{J-1} & \sum_{j=J}^{\infty} p_j \\ 0 & p_0 & \cdots & p_{J-2} & \sum_{j=J-1}^{\infty} p_j \\ \vdots & \vdots & \vdots & \vdots & \vdots \\ 0 & 0 & \cdots & p_0 & \sum_{j=1}^{\infty} p_j \end{bmatrix} \tag{32}$$

Suppose $\pi_j = \lim_{r\to\infty} P\{X_r = j\}, j = 0, 1, \ldots, J$ represent the limiting probability of X_r being in state j after a large number of transitions, it can be given by

$$\pi_j = \sum_{i=0}^{J} \pi_i p_{ij} 0 \le j \le J \tag{33}$$

We can calculate $\pi_j, j = 0, 1, \ldots, J$ by using the fact that $\sum_{j=0}^{J} \pi_j = 1$.

TABLE II
PARAMETERS OF TRACKING AND SEARCHING ACTIVITIES

Task types	Priority	Dwell time	Time window	Update rate
HS	4	6 *ms*	10 *ms*	20 Hz
PT	3	2 *ms*	5 *ms*	10 Hz
CT	2	4 *ms*	5 *ms*	4 Hz
LS	1	2 *ms*	10 *ms*	10 Hz

TABLE III
PARAMETERS OF TARGETS FOR IMAGING

	Distance R (km)	Speed V (m/s)	Heading θ ($^\circ$)	Size S (m^2)
Target 1	10	300	0	517
Target 2	9	260	-20	654
Target 3	8	400	170	174

In the above case, all tasks can only be implemented backwards in the time window of $2W$, the calculated probability of $ROI = 1$ in l-th scheduling interval is very few smaller than the true value, therefore, the minimum probability is

$$P_{ROI=1\,\min} = \sum_{j=1}^{J-1} \pi_j \tag{34}$$

IV. EXPERIMENTS

Next, we will show some simulation experiments to verify the efficiency of the proposed algorithm. In our examples, we only consider high-priority searching, precision tracking, normal tracking, low-priority searching and imaging activities although the algorithm is not restricted to these tasks. In Table II, the priority, dwell time, time window and update rate (frequency of radar request) of the mentioned searching and tracking activities are presented. Table III shows the target parameters of imaging activities. To be intuitively clear, the time sequence of task scheduling with the given parameters is shown in Fig. 2. The goal of the adaptive task scheduling algorithm is to avoid the resources conflict between different tasks and achieve the maximized global utility of MFPAR by implementing each task at the most suitable time. For tracking and searching tasks, the pulse duration $T_p = 1$ μs, center frequency $f_c = 10$ GHz, signal bandwidth $B = 10$ MHz, and pulse repetition frequency $PRF = 1000$ Hz. For imaging tasks, the pulse duration $T_p = 1$ μs, center frequency $f_c = 10$ GHz, signal bandwidth $B = 300$ MHz, and pulse repetition frequency $PRF = 1000$ Hz.

A small amount (100 in this paper) of pulses are transmitted to the imaging targets, we can reconstruct the ISAR image of targets with coarse resolution in the way of filling the missing data zeros to $N_{all} = 1000$ (identical to $T_c = 1$ s) and using two-dimensional matched filtering. The scattering model and the coarse resolution ISAR image of targets are represented in Table IV.

After processing the coarse resolution ISAR images using (7)–(9), and setting the threshold $T_s = 0.2$, $T_k = 0.2$, we can estimate the target size $\hat{S}_k$ and sparsity $\hat{K}_k$. Setting $\rho_{ref} = 0.5$ m, which is the desired azimuthal resolution of the target with datum azimuthal size of $S_{refx} = 25$ m. Supposing the

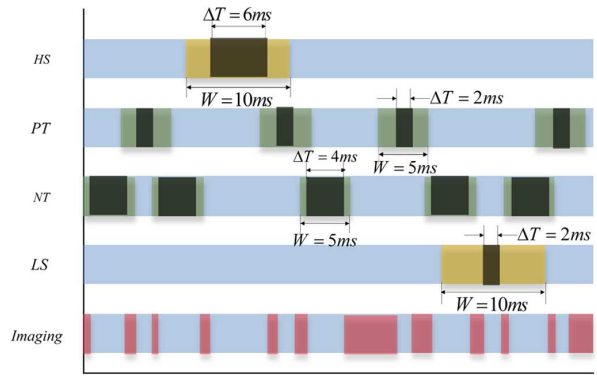

Fig. 2. Time sequence of task scheduling with the given parameters.

TABLE IV
SCATTERING MODEL AND COARSE RESOLUTION ISAR IMAGE OF TARGETS

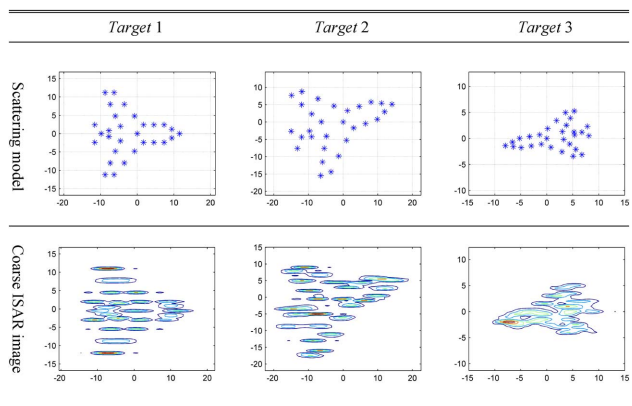

scheduling interval of radar resource is $T = 50$ ms, the imaging priority and the required observation dimension can be calculated according to (10)–(13), where the adjustment coefficient $p_a = 0.4$, $p_b = 0.4$, and $p_c = 0.2$. The results are shown in Table V.

From Table V, we can see that since *Target* 3 is of small size, high speed and moving toward to the radar, it has the highest imaging priority. On the contrary, *Target* 2 is of large size, low speed and moving away from the radar, therefore its priority is the lowest. There are 8 targets for the precision tracking, 25 targets for normal tracking and 3 targets shown in Table III for

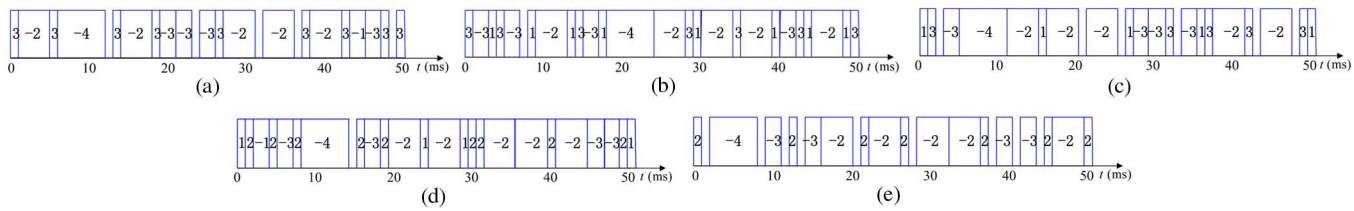

Fig. 3. Scheduling timing diagram. (a) Scheduling timing diagram of *Interval* 1. (b) Scheduling timing diagram of *Interval* 2. (c) Scheduling timing diagram of *Interval* 12. (d) Scheduling timing diagram of *Interval* 13. (e) Scheduling timing diagram of *Interval* 14. The meanings of the numbers in the figures are: −1—LS, −2—CT, −3—PT, −4—HS, 1—Imaging for *Target* 1, 2—Imaging for *Target* 2, 3—Imaging for *Target* 3.

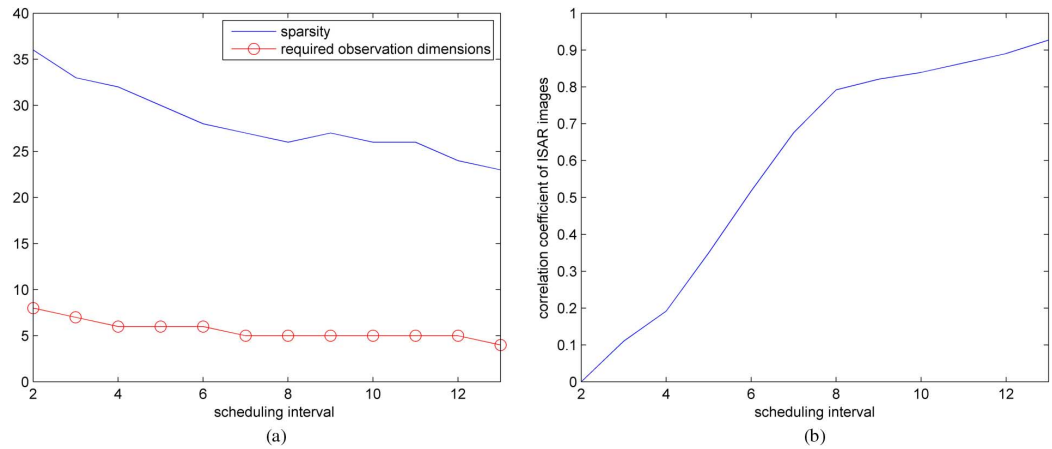

Fig. 4. Adaptive update process of the sparsity estimation and change of correlation coefficient of ISAR images for *Target* 1. (a) Adaptive update process of the sparsity estimation. (b) Change of correlation coefficient of ISAR images.

TABLE V
PRIORITY, REQUIRED OBSERVATION DIMENSIONS IN UNIT SCHEDULING INTERVAL AND OBSERVING TIME

	Target 1	*Target* 2	*Target* 3
Size $\hat{S}_k$ (m^2)	587	754	185
Azimuthal size $\hat{S}_{kx}$ (m)	25.5	29.5	19.5
Sparsity $\hat{K}_k$	50	55	45
Priority $P_{k,0}$	0.6200	0.5472	0.8347
Observation dimensions M'_k	8	9	9

imaging in the working area of the multifunction phased array radar. Based on the initial cognitive results in Table V and choosing the threshold of the correlation coefficient of ISAR images from the adjacent scheduling intervals as $T_\rho = 0.9$, the time resources are allocated according to the scheduling optimization model, where the adjustment coefficient are $\omega_1 = 0.8$, $\omega_2 = 0.1$, and $\omega_3 = 0.1$. Finally the resource scheduling sequence diagram can be acquired as shown in Fig. 3 and the adaptive update process of the sparsity estimation is shown in Fig. 4–6.

The implemented benefit of HS, PT, NT, LS and the three imaging tasks are 0.9000, 0.7222, 0.4944, 0.3222, 0.2379, 0.2053 and 0.2974, respectively.

From Fig. 3–6, we can see that *Target* 3 is of the highest implemented benefit among all the imaging tasks, so the radar will use the vacant aperture between tracking and searching in the 1st scheduling interval to carry out its observation and imaging. After the 12th scheduling interval, the correlation coefficient of ISAR images from the adjacent scheduling intervals is larger than the threshold implying that the task reaches the image quality requirements. Then the priority is set to zero and the task is no longer scheduled in the next scheduling interval. Similarly, the implemented benefit of *Target* 1 is higher than *Target* 2, so the vacant aperture in the 2nd scheduling interval is used for its observation and imaging. After the 13th scheduling interval, the correlation coefficient is larger than the threshold and the task is accomplished. Furthermore, from Fig. 4–6 we can see that as the scheduling times increases, the observation time accumulates constantly, and the estimated value of sparsity decreases accordingly and gradually reach a standstill, while the correlation coefficient of ISAR images increases and achieves to the required image quality finally. This is because as the azimuthal coherent accumulation time increases, the resolution of ISAR imaging improves correspondingly, which makes the sparsity estimation more and more accurate, and the correlation coefficient of ISAR images from the adjacent scheduling intervals higher and higher.

To evaluate the quality of ISAR image by this algorithm, we made a comparison of the proposed algorithm with the traditional ISAR imaging algorithm (continuous full aperture observation for targets with coherent time $T_{c,k}$). The results are shown in Table VI, and the correlation coefficient of ISAR images of each targets from the two algorithms reached to 0.9155, 0.9033 and 0.9426, respectively.

The performance metrics of the traditional scheduling algorithm for phased array radar described in Section III and the adaptive scheduling algorithm based on cognitive ISAR imaging proposed in this paper are compared in Table VII. It is observed that the proposed method can improve each

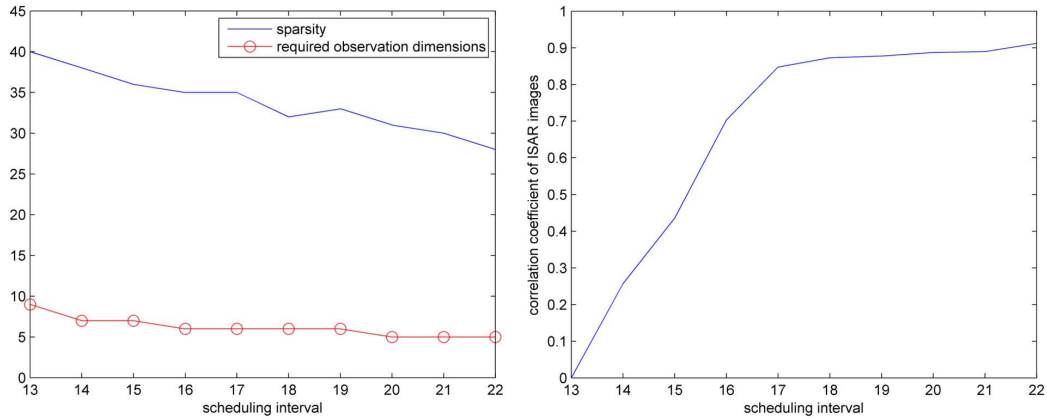

(a) (b)

Fig. 5. Adaptive update process of the sparsity estimation and change of correlation coefficient of ISAR images for *Target* 2. (a) Adaptive update process of the sparsity estimation. (b) Change of correlation coefficient of ISAR images.

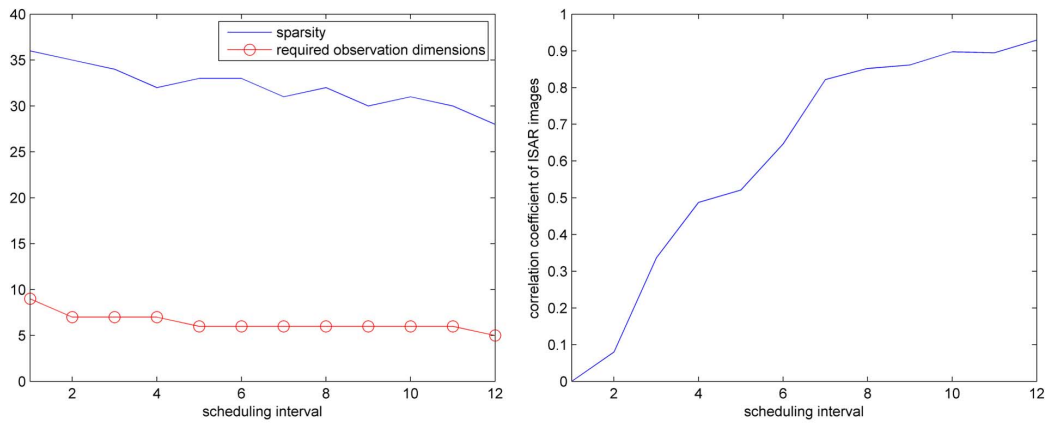

(a) (b)

Fig. 6. Adaptive update process of the sparsity estimation and change of correlation coefficient of ISAR images for *Target* 3. (a) Adaptive update process of the sparsity estimation. (b) Change of correlation coefficient of ISAR images.

TABLE VI
OMPARISON OF IMAGE QUALITY BY DIFFERENT ALGORITHM

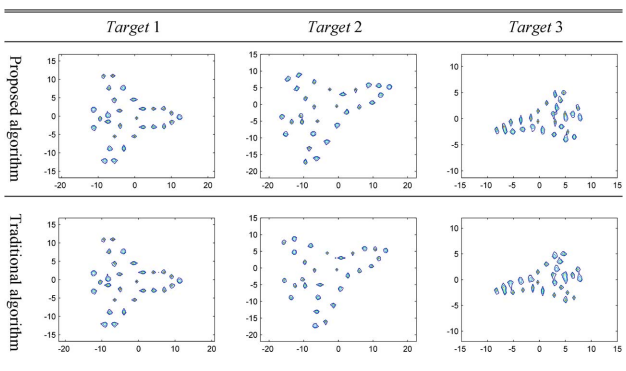

TABLE VII
PARAMETERS OF PERFORMANCE METRICS

	SPI	ROI	TUR
Traditional algorithm	26.50	77.75%	70.00%
Proposed algorithm	29.11	89.21%	87.36%

performance metric, obtaining high quality ISAR image while accomplishing trackinging and searching task, which improves the working efficiency of MFPAR significantly.

TABLE VIII
PROBABILITY OF IMPLEMENTING ALL TASKS

	Scene 1	*Scene* 2	*Scene* 3	*Scene* 4
$P_{ROI=1\min}$	95.32%	98.43%	82.57%	71.71%
$P_{ROI=1}$	97.82%	99.28%	83.33%	72.73%

Next, we discuss the probability of $ROI = 1$ under several different conditions as follows:

Scene 1:

$$N = 3, M = 3, U = 3, G = 3, \Delta T_a = 4, \Delta T_b = 2,$$
$$\Delta T_c = 3, \Delta T_d = 1, M_{all} = 8, W_a = W_b = W_c = W_d = 3$$

Scene 2:

$$N = 3, M = 3, U = 3, G = 3, \Delta T_a = 4, \Delta T_b = 2,$$
$$\Delta T_c = 3, \Delta T_d = 1, M_{all} = 8, W_a = W_b = W_c = W_d = 5$$

Scene 3:

$$N = 4, M = 4, U = 4, G = 4, \Delta T_a = 4, \Delta T_b = 2,$$
$$\Delta T_c = 3, \Delta T_d = 1, M_{all} = 8, W_a = W_b = W_c = W_d = 3$$

Scene 4:

$$N = 3, M = 3, U = 3, G = 3, \Delta T_a = 5, \Delta T_b = 5,$$
$$\Delta T_c = 3, \Delta T_d = 2, M_{all} = 8, W_a = W_b = W_c = W_d = 3$$

where M_{all} is the sum of the required aperture number for all the imaging tasks. The probability of $ROI = 1$ obtained by experiments $P_{ROI=1}$ and calculated according to (33) and (34) $P_{ROI=1\min}$ are both shown in Table VIII.

From Table VIII, we can see that the probability $P_{ROI=1}$ depends on the number of task requests, the dwell time and the time window. Comparison of *Scene* 1 and *Scene* 2 shows that as the time window increases, the probability enhances correspondingly. Further, when the number of tasks and the dwell time increases, the probability decreases accordingly as indicated by the comparison of *Scene* 1 and *Scene* 3, *Scene* 1 and *Scene* 4, respectively.

When the radar echo contains noise, the noise will make the ISAR image worse, which leads to the increase of sparsity estimation value and the required observation dimension. As a result, more resources are required to allocate for the target imaging. Also, the increase of correlation coefficient of ISAR images becomes slower and the correlation coefficient is hard to reach a high value. Therefore, decreasing the threshold of the correlation coefficient of ISAR images is a feasible way when the echo signal contains noise.

It should be noted that the noise only makes the sparsity estimation value larger and the increasing of correlation coefficients slower, which slightly downgrades the performance metrics. But it does not affect the effectiveness of the proposed method and the correctness of the probability analysis of $\mathrm{ROI} = 1$ in a certain scheduling interval.

V. Discussions and Conclusions

In this paper, a novel adaptive scheduling algorithm have been proposed based on the cognitive imaging method for the sparse aperture ISAR, and the performance metrics have been demonstrated. Based on the cognition of the target features, the imaging function is considered in the resource scheduling strategy so that imaging, trackinging and searching tasks can be implemented simultaneously. The simulation results show that the algorithm can accomplish trackinging and searching task effectively as well as obtain high quality ISAR image, thus improving the radar working efficiency significantly. It should be noted that in this paper, we assume that the target is non-maneuvering, in fact, imaging for maneuvering target needs to select optimal imaging time. The smooth time of flight can be selected from the tracing information and be used for target imaging. Due to the lack of real data, we examined the performance of the algorithm using simulation data in this paper. In our future work, we will introduce the algorithm to real data processing and analyze the threshold selection.

Appendix

Conditions1–11 are shown at the bottom of the following pages.

In these conditions, $P_{overlap}(T_{aq}, T_{an_{hs}}, \Delta T_a) = \sum_{x=1}^{-|T_{aq}-T_{an_{hs}}|+W_{aq}+W_{an_{hs}}} \frac{\min(x,\Delta T_a)}{2W_{an_{hs}}}$ represents the occupied time of $A_{n_{hs}}$ within the time window A_q. $T_{aqaq'} = \frac{T_{aq}+T_{aq'}+(W_{aq}-W_{aq'})\cdot\mathrm{sgn}(T_{aq'}-T_{aq})}{2}$ and $W_{aqaq'} = \frac{-|T_{aq}-T_{aq'}|+W_{aq}+W_{aq'}}{2}$ stand for the overlap area of the time window of A_q and $A_{q'}$, where $\mathrm{sgn}(x) = \begin{cases} 1 & x > 0 \\ 0 & x = 0 \\ -1 & x < 0 \end{cases}$. Other symbols follow the same definition criteria.

Condition1:

$$\forall n_{hs} \in \{1,2,\ldots,N_{HS}\} t_0 - W_a < T_{an_{hs}} < T + t_0 - \Delta T_a + W_a,$$
$$\forall m_{pt} \in \{1,2,\ldots,M_{PT}\} t_0 - W_b < T_{bm_{pt}} < T + t_0 - \Delta T_b + W_b,$$
$$\forall u_{nt} \in \{1,2,\ldots,U_{NT}\} t_0 - W_c < T_{cu_{nt}} < T + t_0 - \Delta T_c + W_c,$$
$$\forall g_{ls} \in \{1,2,\ldots,G_{LS}\} t_0 - W_d < T_{dg_{ls}} < T + t_0 - \Delta T_d + W_d$$

Condition2:

$$\forall (q,q') \in \{(q,q') | (q,q') = 1,2,\ldots,N_{HS}, q > q'\}$$
$$|T_{aq} - T_{aq'}| > \Delta T_a +$$
$$\sum_{n_{hs}=1, n_{hs}\neq q,q'}^{N_{HS}} (P_{overlap}(T_{aq}, T_{an_{hs}}, \Delta T_a) + P_{overlap}(T_{aq'}, T_{an_{hs}}, \Delta T_a) - P_{overlap}(T_{aqaq'}, T_{an_{hs}}, \Delta T_a)) +$$
$$\sum_{m_{pt}=1}^{M_{PT}} (P_{overlap}(T_{aq}, T_{bm_{pt}}, \Delta T_b) + P_{overlap}(T_{aq'}, T_{bm_{pt}}, \Delta T_b) - P_{overlap}(T_{aqaq'}, T_{bm_{pt}}, \Delta T_b)) +$$
$$\sum_{u_{nt}=1}^{U_{NT}} (P_{overlap}(T_{aq}, T_{cu_{nt}}, \Delta T_c) + P_{overlap}(T_{aq'}, T_{cu_{nt}}, \Delta T_c) - P_{overlap}(T_{aqaq'}, T_{cu_{nt}}, \Delta T_c)) +$$
$$\sum_{g_{ls}=1}^{G_{LS}} (P_{overlap}(T_{aq}, T_{dg_{ls}}, \Delta T_d) + P_{overlap}(T_{aq'}, T_{dg_{ls}}, \Delta T_d) - P_{overlap}(T_{aqaq'}, T_{dg_{ls}}, \Delta T_d)) -$$
$$P(T_{aq} < T_{aq'}) \cdot \{\min(T_{aq} - 1 - t_0, W_a) + \min(T + t_0 - T_{aq'}, W_a)\} -$$
$$P(T_{aq} > T_{aq'}) \cdot \{\min(T_{aq'} - 1 - t_0, W_a) + \min(T + t_0 - T_{aq}, W_a)\},$$

Condition3:

$$\forall(q,q')\in\{(q,q')|q=1,2,\ldots,G_{LS},q'=1,2,\ldots,U_{NT}\}$$
$$|T_{dq}-T_{cq'}|>P(T_{dq}<T_{cq'})\cdot\Delta T_d+P(T_{dq}>T_{cq'})\cdot\Delta T_c+$$
$$\sum_{n_{hs}=1}^{N_{HS}}(P_{overlap}(T_{dq},T_{an_{hs}},\Delta T_a)+P_{overlap}(T_{cq'},T_{an_{hs}},\Delta T_a)-P_{overlap}(T_{dqcq'},T_{an_{hs}},\Delta T_a))+$$
$$\sum_{m_{pt}=1}^{M_{PT}}(P_{overlap}(T_{dq},T_{bm_{pt}},\Delta T_b)+P_{overlap}(T_{cq'},T_{bm_{pt}},\Delta T_b)-P_{overlap}(T_{dqcq'},T_{bm_{pt}},\Delta T_b))+$$
$$\sum_{u_{nt}=1,u_{nt}\neq q'}^{U_{NT}}(P_{overlap}(T_{dq},T_{cu_{nt}},\Delta T_c)+P_{overlap}(T_{cq'},T_{cu_{nt}},\Delta T_c)-P_{overlap}(T_{dqcq'},T_{cu_{nt}},\Delta T_c))+$$
$$\sum_{g_{ls}=1,g_{ls}\neq q}^{G_{LS}}(P_{overlap}(T_{dq},T_{dg_{ls}},\Delta T_d)+P_{overlap}(T_{cq'},T_{dg_{ls}},\Delta T_d)-P_{overlap}(T_{dqcq'},T_{dg_{ls}},\Delta T_d))-$$
$$P(T_{dq}<T_{cq'})\cdot\{\min(T_{dq}-1-t_0,W_d)+\min(T+t_0-T_{cq'},W_c)\}-$$
$$P(T_{dq}>T_{cq'})\cdot\{\min(T_{cq'}-1-t_0,W_c)+\min(T+t_0-T_{dq},W_d)\},$$

Condition4:

$$\forall(q,q')\in\{(q,q')|q=1,2,\ldots,U_{NT},q'=1,2,\ldots,N_{HS}\}$$
$$|T_{cq}-T_{aq'}|>P(T_{cq}<T_{aq'})\cdot\Delta T_c+P(T_{cq}>T_{aq'})\cdot\Delta T_a+$$
$$\sum_{n_{hs}=1,n_{hs}\neq q'}^{N_{HS}}(P_{overlap}(T_{cq},T_{an_{hs}},\Delta T_a)+P_{overlap}(T_{aq'},T_{an_{hs}},\Delta T_a)-P_{overlap}(T_{cqaq'},T_{an_{hs}},\Delta T_a))+$$
$$\sum_{m_{ht}=1}^{M_{HT}}(P_{overlap}(T_{cq},T_{bm_{ht}},\Delta T_b)+P_{overlap}(T_{aq'},T_{bm_{ht}},\Delta T_b)-P_{overlap}(T_{cqaq'},T_{bm_{ht}},\Delta T_b))+$$
$$\sum_{u_{nt}=1,u_{nt}\neq q}^{U_{NT}}(P_{overlap}(T_{cq},T_{cu_{nt}},\Delta T_c)+P_{overlap}(T_{aq'},T_{cu_{nt}},\Delta T_c)-P_{overlap}(T_{cqaq'},T_{cu_{nt}},\Delta T_c))+$$
$$\sum_{g_{ls}=1}^{G_{LS}}(P_{overlap}(T_{cq},T_{dg_{ls}},\Delta T_d)+P_{overlap}(T_{aq'},T_{dg_{ls}},\Delta T_d)-P_{overlap}(T_{cqaq'},T_{dg_{ls}},\Delta T_d))-$$
$$P(T_{cq}<T_{aq'})\cdot\{\min(T_{cq}-1-t_0,W_c)+\min(T+t_0-T_{aq'},W_a)\}-$$
$$P(T_{cq}>T_{aq'})\cdot\{\min(T_{aq'}-1-t_0,W_a)+\min(T+t_0-T_{cq},W_c)\},$$

Condition5:

$$\forall(q,q')\in\{(q,q')|q=1,2,\ldots,G_{LS},q'=1,2,\ldots,N_{HS}\}$$
$$|T_{dq}-T_{aq'}|>P(T_{dq}<T_{aq'})\cdot\Delta T_d+P(T_{dq}>T_{aq'})\cdot\Delta T_a+$$
$$\sum_{n_{hs}=1,n_{hs}\neq q'}^{N_{HS}}(P_{overlap}(T_{dq},T_{an_{hs}},\Delta T_a)+P_{overlap}(T_{aq'},T_{an_{hs}},\Delta T_a)-P_{overlap}(T_{dqaq'},T_{an_{hs}},\Delta T_a))+$$
$$\sum_{m_{pt}=1}^{M_{PT}}(P_{overlap}(T_{dq},T_{bm_{pt}},\Delta T_b)+P_{overlap}(T_{aq'},T_{bm_{pt}},\Delta T_b)-P_{overlap}(T_{dqaq'},T_{bm_{pt}},\Delta T_b))+$$
$$\sum_{u_{nt}=1}^{U_{NT}}(P_{overlap}(T_{dq},T_{cu_{nt}},\Delta T_c)+P_{overlap}(T_{aq'},T_{cu_{nt}},\Delta T_c)-P_{overlap}(T_{dqaq'},T_{cu_{nt}},\Delta T_c))+$$
$$\sum_{g_{ls}=1,g_{ls}\neq q}^{G_{LS}}(P_{overlap}(T_{dq},T_{dg_{ls}},\Delta T_d)+P_{overlap}(T_{aq'},T_{dg_{ls}},\Delta T_d)-P_{overlap}(T_{dqaq'},T_{dg_{ls}},\Delta T_d))-$$
$$P(T_{dq}<T_{aq'})\cdot\{\min(T_{dq}-1-t_0,W_d)+\min(T+t_0-T_{aq'},W_a)\}-$$
$$P(T_{dq}>T_{aq'})\cdot\{\min(T_{aq'}-1-t_0,W_a)+\min(T+t_0-T_{dq},W_d)\},$$

Condition6:

$$\forall(q,q') \in \{(q,q')|(q,q') = 1,2,\ldots,M, q > q'\}$$

$$|T_{bq} - T_{bq'}| > \Delta T_b +$$

$$\sum_{n_{hs}=1}^{N_{HS}} (P_{overlap}(T_{bq}, T_{an_{hs}}, \Delta T_a) + P_{overlap}(T_{bq'}, T_{an_{hs}}, \Delta T_a) - P_{overlap}(T_{bqbq'}, T_{an_{hs}}, \Delta T_a)) +$$

$$\sum_{m_{ht}=1, m_{ht}\neq q,q'}^{M_{HT}} (P_{overlap}(T_{bq}, T_{bm_{ht}}, \Delta T_b) + P_{overlap}(T_{bq'}, T_{bm_{ht}}, \Delta T_b) - P_{overlap}(T_{bqbq'}, T_{bm_{ht}}, \Delta T_b)) +$$

$$\sum_{u_{nt}=1}^{U_{NT}} (P_{overlap}(T_{bq}, T_{cu_{nt}}, \Delta T_c) + P_{overlap}(T_{bq'}, T_{cu_{nt}}, \Delta T_c) - P_{overlap}(T_{bqbq'}, T_{cu_{nt}}.\Delta T_c)) +$$

$$\sum_{g_{ls}=1}^{G_{LS}} (P_{overlap}(T_{bq}, T_{dg_{ls}}, \Delta T_d) + P_{overlap}(T_{bq'}, T_{dg_{ls}}, \Delta T_d) - P_{overlap}(T_{bqbq'}, T_{dg_{ls}}, \Delta T_d)) -$$

$$P(T_{bq} < T_{bq'}) \cdot \{\min(T_{bq} - 1 - t_0, W_b) + \min(T + t_0 - T_{bq'}, W_b)\} -$$

$$P(T_{bq} > T_{bq'}) \cdot \{\min(T_{bq'} - 1 - t_0, W_b) + \min(T + t_0 - T_{bq}, W_b)\},$$

Condition7:

$$\forall(q,q') \in \{(q,q')|q = 1,2,\ldots,U_{NT}, q' = 1,2,\ldots,M_{HT}\}$$

$$|T_{cq} - T_{bq'}| > P(T_{cq} < T_{bq'}) \cdot \Delta T_c + P(T_{cq} > T_{bq'}) \cdot \Delta T_b +$$

$$\sum_{n_{hs}=1}^{N_{HS}} (P_{overlap}(T_{cq}, T_{an_{hs}}, \Delta T_a) + P_{overlap}(T_{bq'}, T_{an_{hs}}, \Delta T_a) - P_{overlap}(T_{cqbq'}, T_{an_{hs}}, \Delta T_a)) +$$

$$\sum_{m_{pt}=1, m_{pt}\neq q'}^{M_{PT}} (P_{overlap}(T_{cq}, T_{bm_{pt}}, \Delta T_b) + P_{overlap}(T_{bq'}, T_{bm_{pt}}, \Delta T_b) - P_{overlap}(T_{cqbq'}, T_{bm_{pt}}, \Delta T_b)) +$$

$$\sum_{u_{nt}=1, u_{nt}\neq q}^{U_{NT}} (P_{overlap}(T_{cq}, T_{cu_{nt}}, \Delta T_c) + P_{overlap}(T_{bq'}, T_{cu_{nt}}, \Delta T_c) - P_{overlap}(T_{cqbq'}, T_{cu_{nt}}, \Delta T_c)) +$$

$$\sum_{g_{ls}=1}^{G_{LS}} (P_{overlap}(T_{cq}, T_{dg_{ls}}, \Delta T_d) + P_{overlap}(T_{bq'}, T_{dg_{ls}}, \Delta T_d) - P_{overlap}(T_{cqbq'}, T_{dg_{ls}}, \Delta T_d)) -$$

$$P(T_{cq} < T_{bq'}) \cdot \{\min(T_{cq} - 1 - t_0, W_c) + \min(T + t_0 - T_{bq'}, W_b)\} -$$

$$P(T_{cq} > T_{bq'}) \cdot \{\min(T_{bq'} - 1 - t_0, W_b) + \min(T + t_0 - T_{cq}, W_c)\},$$

Condition8:

$$\forall(q,q') \in \{(q,q')|(q,q') = 1,2,\ldots,G, q > q'\}$$

$$|T_{dq} - T_{dq'}| > \Delta T_d +$$

$$\sum_{n_{hs}=1}^{N_{HS}} (P_{overlap}(T_{dq}, T_{an_{hs}}, \Delta T_a) + P_{overlap}(T_{dq'}, T_{an_{hs}}, \Delta T_a) - P_{overlap}(T_{dqdq'}, T_{an_{hs}}, \Delta T_a)) +$$

$$\sum_{m_{pt}=1}^{M_{PT}} (P_{overlap}(T_{dq}, T_{bm_{pt}}, \Delta T_b) + P_{overlap}(T_{dq'}, T_{bm_{pt}}, \Delta T_b) - P_{overlap}(T_{dqdq'}, T_{bm_{pt}}, \Delta T_b)) +$$

$$\sum_{u_{nt}=1}^{U_{NT}} (P_{overlap}(T_{dq}, T_{cu_{nt}}, \Delta T_c) + P_{overlap}(T_{dq'}, T_{cu_{nt}}, \Delta T_c) - P_{overlap}(T_{dqdq'}, T_{cu_{nt}}, \Delta T_c)) +$$

$$\sum_{g_{ls}=1, g_{ls}\neq q,q'}^{G_{LS}} (P_{overlap}(T_{dq}, T_{dg_{ls}}, \Delta T_d) + P_{overlap}(T_{dq'}, T_{dg_{ls}}, \Delta T_d) - P_{overlap}(T_{dqdq'}, T_{dg_{ls}}, \Delta T_d)) -$$

$$P(T_{dq} < T_{dq'}) \cdot \{\min(T_{dq} - 1 - t_0, W_d) + \min(T + t_0 - T_{dq'}, W_d)\} -$$

$$P(T_{dq} > T_{dq'}) \cdot \{\min(T_{dq'} - 1 - t_0, W_d) + \min(T + t_0 - T_{dq}, W_d)\}$$

Condition9:

$$\forall(q,q')\in\{(q,q')|(q,q')=1,2,\ldots,U_{NT},q>q'\}$$
$$|T_{cq}-T_{cq'}|>\Delta T_c+$$
$$\sum_{n_{hs}=1}^{N_{HS}}(P_{overlap}(T_{cq},T_{an_{hs}},\Delta T_a)+P_{overlap}(T_{cq'},T_{an_{hs}},\Delta T_a)-P_{overlap}(T_{cqcq'},T_{an_{hs}},\Delta T_a))+$$
$$\sum_{m_{pt}=1}^{M_{PT}}(P_{overlap}(T_{cq},T_{bm_{pt}},\Delta T_b)+P_{overlap}(T_{cq'},T_{bm_{pt}},\Delta T_b)-P_{overlap}(T_{cqcq'},T_{bm_{pt}},\Delta T_b))+$$
$$\sum_{u_{nt}=1,u_{nt}\neq q,q'}^{U_{NT}}(P_{overlap}(T_{cq},T_{cu_{nt}},\Delta T_c)+P_{overlap}(T_{cq'},T_{cu_{nt}},\Delta T_c)-P_{overlap}(T_{cqcq'},T_{cu_{nt}},\Delta T_c))+$$
$$\sum_{g_{ls}=1}^{G_{LS}}(P_{overlap}(T_{cq},T_{dg_{ls}},\Delta T_d)+P_{overlap}(T_{cq'},T_{dg_{ls}},\Delta T_d)-P_{overlap}(T_{cqcq'},T_{dg_{ls}},\Delta T_d))-$$
$$P(T_{cq}<T_{cq'})\cdot\{\min(T_{cq}-1-t_0,W_c)+\min(T+t_0-T_{cq'},W_c)\}-$$
$$P(T_{cq}>T_{cq'})\cdot\{\min(T_{cq'}-1-t_0,W_c)+\min(T+t_0-T_{cq},W_c)\},$$

Condition10:

$$\forall(q,q')\in\{(q,q')|q=1,2,\ldots,M_{PT},q'=1,2,\ldots,N_{HS}\}$$
$$|T_{bq}-T_{aq'}|>P(T_{bq}<T_{aq'})\cdot\Delta T_b+P(T_{bq}>T_{aq'})\cdot\Delta T_a+$$
$$\sum_{n_{hs}=1,n_{hs}\neq q'}^{N_{HS}}(P_{overlap}(T_{bq},T_{an_{hs}},\Delta T_a)+P_{overlap}(T_{aq'},T_{an_{hs}},\Delta T_a)-P_{overlap}(T_{bqaq'},T_{an_{hs}},\Delta T_a))+$$
$$\sum_{m_{pt}=1,m_{pt}\neq p}^{M_{PT}}(P_{overlap}(T_{bq},T_{bm_{pt}},\Delta T_b)+P_{overlap}(T_{aq'},T_{bm_{pt}},\Delta T_b)-P_{overlap}(T_{bqaq'},T_{bm_{pt}},\Delta T_b))+$$
$$\sum_{u_{nt}=1}^{U_{NT}}(P_{overlap}(T_{bq},T_{cu_{nt}},\Delta T_c)+P_{overlap}(T_{aq'},T_{cu_{nt}},\Delta T_c)-P_{overlap}(T_{bqaq'},T_{cu_{nt}},\Delta T_c))+$$
$$\sum_{g_{ls}=1}^{G_{LS}}(P_{overlap}(T_{bq},T_{dg_{ls}},\Delta T_d)+P_{overlap}(T_{aq'},T_{dg_{ls}},\Delta T_d)-P_{overlap}(T_{bqaq'},T_{dg_{ls}},\Delta T_d))-$$
$$P(T_{bq}<T_{aq'})\cdot\{\min(T_{bq}-1-t_0,W_b)+\min(T+t_0-T_{aq'},W_a)\}-$$
$$P(T_{bq}>T_{aq'})\cdot\{\min(T_{aq'}-1-t_0,W_a)+\min(T+t_0-T_{bq},W_b)\},$$

Condition11:

$$\forall(q,q')\in\{(q,q')|q=1,2,\ldots,G_{LS},q'=1,2,\ldots,M_{HT}\}$$
$$|T_{dq}-T_{bq'}|>P(T_{dq}<T_{bq'})\cdot\Delta T_d+P(T_{dq}>T_{bq'})\cdot\Delta T_b+$$
$$\sum_{n_{hs}=1}^{N_{HS}}(P_{overlap}(T_{dq},T_{an_{hs}},\Delta T_a)+P_{overlap}(T_{bq'},T_{an_{hs}},\Delta T_a)-P_{overlap}(T_{dqbq'},T_{an_{hs}},\Delta T_a))+$$
$$\sum_{m_{pt}=1,m_{pt}\neq q'}^{M_{PT}}(P_{overlap}(T_{dq},T_{bm_{pt}},\Delta T_b)+P_{overlap}(T_{bq'},T_{bm_{pt}},\Delta T_b)-P_{overlap}(T_{dqbq'},T_{bm_{pt}},\Delta T_b))+$$
$$\sum_{u_{nt}=1}^{U_{NT}}(P_{overlap}(T_{dq},T_{cu_{nt}},\Delta T_c)+P_{overlap}(T_{bq'},T_{cu_{nt}},\Delta T_c)-P_{overlap}(T_{dqbq'},T_{cu_{nt}},\Delta T_c))+$$
$$\sum_{g_{ls}=1,g_{ls}\neq q}^{G_{LS}}(P_{overlap}(T_{dq},T_{dg_{ls}},\Delta T_d)+P_{overlap}(T_{bq'},T_{dg_{ls}},\Delta T_d)-P_{overlap}(T_{dqbq'},T_{dg_{ls}},\Delta T_d))-$$
$$P(T_{dq}<T_{bq'})\cdot\{\min(T_{dq}-1-t_0,W_d)+\min(T+t_0-T_{bq'},W_b)\}-$$
$$P(T_{dq}>T_{bq'})\cdot\{\min(T_{bq'}-1-t_0,W_b)+\min(T+t_0-T_{dq},W_d)\},$$

REFERENCES

[1] C. G. Lee, P. S. Kang, C. S. Shih, and L. Sha, "Radar dwell scheduling considering physical characteristics of phased array antenna," in *Proc. 24th IEEE Real-Time Systems Symp.*, Mexico, 2003, pp. 14–24.

[2] D. S. Jang, H. L. Choi, and J. E. Roh, "A Time-Window-Based task scheduling approach for multi-function phased array Radars," in *Proc. 2011 Control, Autom., Systems*, Kintex, 2011, pp. 1250–1255.

[3] S. Gopalakrishnan, M. Caccamo, C. S. Shih, C. G. Lee, and L. Sha, "Finite-horizon scheduling of radar dwells with online template construction," in *Proc. 25th IEEE Real-Time Systems Symp.* , Lisbon, Portugal, 2004, pp. 23–33.

[4] C. S. Shih, S. Gopalakrishnan, P. Ganti, M. Caccamo, and L. Sha, "Template-based real-time dwell scheduling with energy constraint," in *9th IEEE Real-Time and Embedded Technology and Applications Symposium*, Washington DC, 2003, pp. 19–27.

[5] C. G. Lee, "A novel framework for quality-aware resource management in phased array radar systems," in *11th IEEE Real-Time and Embedded Technology and Applications Symposium*, San Francisco, 2005, pp. 322–331.

[6] J. Yang, G. Dong, Y. Peng, Y. Yamaguchi, and H. Yamada, "Generalized optimization of polarimetric contrast enhancement," *IEEE Geosci. Remote Sensing Let.*, vol. 1, no. 3, pp. 171–174, Jul. 2004.

[7] K. Dogancay, "Relationship between gometric translations and TL S estimation bias in bearings-only target localization," *IEEE Trans. Signal Processing*, vol. 56, no. 3, pp. 1005–1017, Mar. 2008.

[8] D. L. Donoho, "Compressed sensing," *IEEE Trans. Information Theory*, vol. 52, no. 4, pp. 1289–1306, Apr. 2006.

[9] E. J. Cand'es and T. Tao, "Near-optimal signal recovery from random projections: Universal encoding strategies," *IEEE Trans. Inform Theory*, vol. 52, no. 12, pp. 5406–5425, Dec. 2006.

[10] L. Zhang, Z. J. Qiao, M. D. Xing, Y. C. Li, and Z. Bao, "High resolution ISAR imaging with sparse stepped-frequency waveforms," *IEEE Trans. Geoscience and Remote Sensing*, vol. 49, no. 11, pp. 4630–4651, Nov. 2011.

[11] W. An, Y. Cui, W. Zhang, and J. Yang, "Data compression for multilook polarimetric SAR Data," *IEEE Geosci. and Remote Sensing Lett.*, vol. 6, no. 3, pp. 476–480, July 2009.

[12] L. Zhang, M. Xing, C. W. Qiu, J. Li, and Z. Bao, "Achieving higher resolution ISAR imaging with limited pulses via compressed sampling," *IEEE. Geosci. Remote Sens. Lett.*, vol. 6, no. 3, pp. 567–571, July 2009.

[13] Y. Luo, Q. Zhang, W. Hong, and Y. R. Wu, "Waveform design and high-resolution imaging of cognitive radar based on compressive sensing," *Sci China Inf. Sci*, vol. 55, no. 11, pp. 2590–2603, Nov. 2012.

[14] F. Zhu, Q. Zhang, Y. Luo, K. M. Li, and F. F. Gu, "A novel cognitive ISAR imaging method with random stepped frequency chirp signal," *Sci China Inf. Sci*, vol. 55, no. 8, pp. 1910–1924, Aug. 2012.

[15] D. Y. Zhu, Y. Li, and X. Yu *et al.*, "Compressed ISAR sutofocusing: Experimental results," in *2012 IEEE Radar Conference*, Atlanta, 2012, pp. 425–430.

[16] S. Shah, Y. Yu, and A. Petropulu, "Step-frequency Radar with compressive sampling (SFR-CS)," in *IEEE International Conference on Acoustics, Speech and Signal Processing*, Dallas, 2010, pp. 1686–1689.

[17] R. Baraniuk, "A lecture on compressive sensing," *IEEE Trans.Signal Processing Magazine*, vol. 24, no. 4, pp. 118–121, July 2007.

[18] H. Rauhut, K. Schnass, and P. Vandergheynst, "Compressed sensing and redundant dictionaries," *IEEE Trans. Information Theory*, vol. 54, no. 5, pp. 2210–2219, May 2008.

[19] D. Needell and J. A. Tropp, "CoSaMP: Iterative signal recovery from incomplete and inaccurate samples," *Appl Comp Harmonic Anal*, vol. 26, no. 3, pp. 301–321, May 2009.

[20] J. A. Tropp and A. C. Gilbert, "Signal recovery from random measurements via orthogonal matching pursuit," *IEEE Trans. Information Theory*, vol. 53, no. 12, pp. 4655–4666, Dec. 2007.

[21] H. Rauhut, "Stability results for random sampling of sparse trigonometric polynomials," *IEEE Trans. Information Theory*, vol. 54, no. 12, pp. 5661–5670, Dec. 2008.

[22] Y. Luo, Q. Zhang, and C. W. Qiu *et al.*, "Micro-Doppler feature extraction for wideband imaging Radar based on complex image orthogonal matching pursuit decomposition," *IET Radar Sonar and Navigation*, vol. 7, no. 8, pp. 914–924, Oct. 2013.

[23] Z. Guang, J. B. Lu, and W. D. Hu, "Research on adaptive scheduling algorithm for multifunction phased array radar," *Modern Radar*, vol. 26, no. 6, pp. 14–18, June 2004.

[24] T. W. Kuo, Y. S. Chao, C. F. Kuo, C. Chang, and Y. L. Su, "Real-time dwell scheduling of component-oriented phased array*Radars*," *IEEE Trans. Computers*, vol. 54, no. 1, pp. 47–60, Jan. 2005.

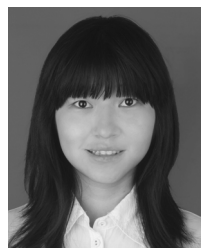

Yijun Chen was born in Shaanxi, China, in 1989. She received the M.S. degree in electrical engineering from the Institute of Information and Navigation, Air Force Engineering University (AFEU), Xi'an, China in 2013, where she is currently working toward the Ph.D. degree in electrical engineering.

She is currently with the Radar and Signal Processing Laboratory, Institute of Information and Navigation, AFEU, and with the Collaborative Innovation Center of Information Sensing and Understanding. Her research interests include signal processing and cognitive radar.

Qun Zhang (M'02–SM'07) received the M.S. degree in mathematics from Shaanxi Normal University, Xi'an, China, in 1988 and the Ph.D. degree in electrical engineering from Xidian University, Xi'an, in 2001.

He was a Research Engineer from 2001 to 2003 and a Research Fellow from 2005 to 2006 with the Department of Electrical and Computer Engineering, National University of Singapore, Singapore. He has published over 200 papers on journals and conferences. His main research interests include signal processing, clutter suppression, and its application in SAR and ISAR.

Ning Yuan (M'05–SM'07) received her B.Sc. and M. Sc. degrees in Electrical Engineering from University of Electronic Science and Technology of China, Chengdu, China in 1993 and 1996, respectively and the Ph.D. degree in electrical engineering from Xidian University in 1999.

From Sept., 1999 to July, 2000, she worked as a Postdoctoral-Fellow in Telecommunications and Industrial Physics, CSIRO, Sydney, Australia. From Aug. 2000 to June 2002, she was a research fellow in National University of Singapore. From July 2002 to June 2007, she was a Research Scientist in Temasek Laboratories. From July 2007 to March 2012, she was a Research Assistant Professor in Department of Electrical and Computer Engineering, University of Houston. Since March 2012, she is a RF Electromagnetic Engineer in Qualcomm, San Diego. Her main research interests include computational electromagnetics, electrical well logging, RF passive components design for integrated circuits etc.

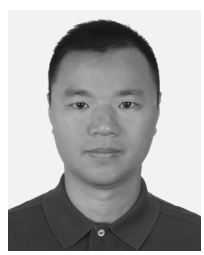

Ying Luo (M'14) was born in Hunan, China, in 1984. He received his MS degree in electrical engineering from the Institute of Telecommunication Engineering, Air Force Engineering University (AFEU), Xi'an, China, in 2008, and the PhD degree in electrical engineering from AFEU, Xi'an, in 2013.

He is currently working in National Laboratory of Radar Signal Processing, Xidian University as a Postdoctoral Fellow, and is also an Adjunct Research Fellow with the Key Laboratory for Information Science of Electromagnetic Waves (Ministry of Education), Fudan University. He has published over 60 papers on journals and conferences. Two of these papers won the First-grade Prize of Shaanxi Natural Science Excellent Academic Paper in 2010 and 2013, respectively. His research interests include signal processing and auto target recognition (ATR) in SAR and ISAR.

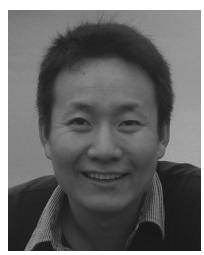

Hao Lou was born in Henan, China, in 1984. He received the M.S. degree in communication engineering from the School of Electronic Science and Engineering, National University of Defense Technology, Changsha, China in 2008.

He is currently working toward the Ph.D. degree in electrical engineering with the Radar and Signal Processing Laboratory, Institute of Information and Navigation, AFEU. His research interests include radar and communication signal processing.